View Article Online
View Journal

Journal of Materials Chemistry A

Accepted Manuscript

This article can be cited before page numbers have been issued, to do this please use: J. Guo, C. Wu, J. Zhang, P. Yan, J. Tian, T. Taylor Isimjan and X. Yang, *J. Mater. Chem. A*, 2019, DOI: 10.1039/C8TA10695A.

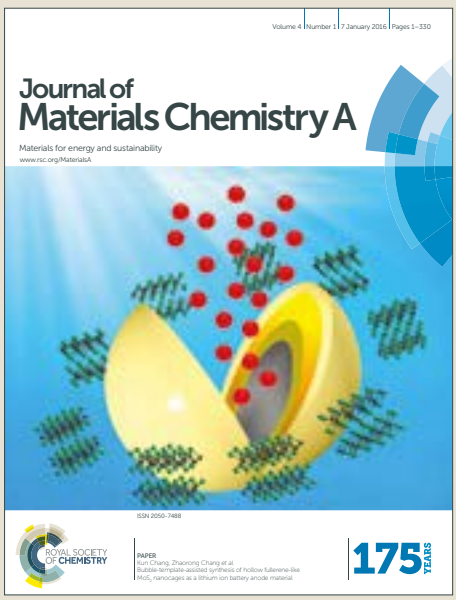

This is an Accepted Manuscript, which has been through the Royal Society of Chemistry peer review process and has been accepted for publication.

Accepted Manuscripts are published online shortly after acceptance, before technical editing, formatting and proof reading. Using this free service, authors can make their results available to the community, in citable form, before we publish the edited article. We will replace this Accepted Manuscript with the edited and formatted Advance Article as soon as it is available.

You can find more information about Accepted Manuscripts in the author guidelines.

Please note that technical editing may introduce minor changes to the text and/or graphics, which may alter content. The journal's standard Terms & Conditions and the ethical guidelines, outlined in our author and reviewer resource centre, still apply. In no event shall the Royal Society of Chemistry be held responsible for any errors or omissions in this Accepted Manuscript or any consequences arising from the use of any information it contains.

ROYAL SOCIETY OF CHEMISTRY

rsc.li/materials-a

View Article Online
DOI: 10.1039/C9TA10695A

Hierarchically Structured Rague-Like RuP_3-CoP Arrays as Robust Catalyst Synergistically Promoting Hydrogen Generation

Jingya Guo,[†] *Chongbei Wu,*[†] *Jifang Zhang,*[†] *Puxuan Yan,*[†] *Jianniao Tian,*[†] *Tayirjan Taylor Isimjan,*,*[‡] *Xiulin Yang*,*[†]

[†]Key Laboratory for the Chemistry and Molecular Engineering of Medicinal Resources (Ministry of Education of China), College of Chemistry and Pharmacy, Guangxi Normal University, Guilin 541004, People's Republic of China

[‡]Saudi Arabia Basic Industries on (SABIC) at King Abdullah University of Science and Technology (KAUST)

E-mail: xiulin.yang@kaust.edu.sa; isimjant@sabic.com

View Article Online
DOI: 10.1039/C8TA10695A

Abstract

Designing a highly active and stable catalyst for $NaBH_4$ hydrolysis is a key step towards overcoming the challenges of hydrogen storage. Herein, we have developed a controllable strategy to fabricate a series of hierarchically structured cobalt-ruthenium-phosphide arrays on nickel foam (Co-Ru-P@NF) as a highly efficient and stable catalyst for hydrogen generation from $NaBH_4$ hydrolysis in alkaline media. SEM and TEM analyses show that the interconnected rague-like Co-Ru-P arrays are vertically grown on the surface of Ni foam, together with uniformly distributed RuP_3 nanoclusters on the surface of CoP nanosheet. More importantly, the optimized Co-Ru-P@NF catalyst exhibits an outstanding catalytic performance on $NaBH_4$ hydrolysis in alkaline media with a high turnover frequency (TOF) of 2123.6 mol_{H2} min^{-1} mol_{Ru}^{-1} at 25 °C, which is one of the highest known so far. Furthermore, the exceptional catalytic performance is in line with the outcome of the low activation energy (40.3 kJ mol^{-1}). Additionally, the catalyst also shows a high stability with less than 8.0% lost after 5 consecutive cycles. The superior catalytic performance is ascribed to the synergetic effect between RuP_3 and CoP species resulting in a significant electron transfer effect, together with the unique morphologies associated to a large specific surface area and open-channels for effective solute transport/adsorption and H_2 gas emissions.

Keywords: CoP nanosheet; RuP_3 nanoclusters; Synergistic effect; $NaBH_4$ hydrolysis; Hydrogen generation

View Article Online
DOI: 10.1039/C8TA10695A

1. Introduction

Dealing with the continuously growing energy demand resulting from the fossil fuel depletion and a related environmental crisis is prompting vigorous research on the field of clean and sustainable alternative energy sources.[1-3] Molecule hydrogen with the highest gravimetric energy density (120 MJ/kg) is regarded as a promising candidate.[4-6] However, H_2 storage and transportation are two main hindrances to launch a H_2 economy.[7-9] The H_2 can be stored both in physical and chemical methods where the H_2 either is adsorbed on highly porous materials such as MOFs and porous carbon which requires extremely low temperature or stored as metal-hydride complexes including boron hydrides ($NaBH_4$, NH_3BH_3 and $LiBH_4$) which has the advantages of high H_2 content (10~20%), high water solubility and stability at room temperature as well as non-toxicity.[10-12] Nevertheless, the boron hydrides hydrolysis generally suffer from sluggish kinetics.[13] Therefore, developing a low cost and high-performance catalyst become an essential step to promote the H_2 storage through boron hydrides. Although the noble metal catalysts such as such as Pt/CeO_2-$Co_7Ni_2O_x$,[14] Pd/PD-ZIF-67,[15] Pt/3D SiC,[16] $Pt_{58}Ni_{33}Au_9$,[17] Pt/mesoporous silica,[18] Ru@SiO_2,[19] Ni-Ru,[20] Rh/Ni BNPs,[21] $Co_{0.8}$-$Ag_{0.2}$-B,[22] *etc*. exhibit the high catalytic performances, they also limited by the cost. As a result, developing the transition metal (Co, Fe, and Ni) based catalysts become the main focus on boron hydride hydrolysis. The recent studies reveal a significant enhancement in the catalytic performance of the transition metal catalyst by incorporating foreign elements including B and P.[23-26] The improvement of the catalytic performance could be due to electron transfer from B or P to the vacant d-orbital of the metal and the electron enriched metal sites further donate the electrons to the surface attached hydrogen atoms thereby accelerates detachment of the surface adsorbed hydrogen atoms.[27] Furthermore, for metal phosphate, in particular, introducing additional foreign metals can further increase the catalytic performance.[28, 29] However, the actual catalytic performance is largely altered by the catalyst preparations, microstructure engineering, surface

View Article Online
DOI: 10.1039/C8TA10695A

area, and the catalyst support. In general, the porous supports such as nickel foam (NF), copper foam, titanium sheet, porous carbon, Al_2O_3, SiO_2, TiO_2 not only supply high surface area but also inhabit the catalyst aggregation thereby improve both activity and stability.[30-33] Compare to powder catalyst, the metal sheet supported catalysts can be easily separated from the solution and used as on/off switch for on-demand hydrogen production.[34] Liu and co-workers found that CoP nanowire array integrated on Ti mesh showed a high hydrogen generation rate for hydrolytic dehydrogenation of $NaBH_4$ in alkaline solutions.[34] Moreover, Sun and co-workers also reported that the Fe-doped CoP nanoarray on Ti foil exhibited high hydrogen generation rate and low activation energy for hydrolytic dehydrogenation of $NaBH_4$ in basic media.[29] Recently, NF support attracted a lot of attention due to the distinguished features such as three-dimensional reticular configuration, high surface area, high flexibility and low cost.[8, 35]

Herein, we have developed a facile and controllable strategy to synthesize a novel RuP_3 coated CoP on NF hybrid catalyst where the cheapest noble metal Ru[36] was used in a small quantity in order to minimize the cost. X-ray diffraction patterns indicate that the RuP_3 and CoP species are formed, and the contents of Ru and Co in the optimized catalyst are indicated to be $Co_{0.991}Ru_{0.09}P$ by ICP-AES. SEM and TEM demonstrate that rague-like CoP arrays are grown on the skeleton of NF, and RuP_3 nanoclusters are uniformly dispersed on the CoP nanosheet surface. The optimized Co-Ru-P@NF catalyst exhibits an outstanding catalytic performance and high stability for $NaBH_4$ hydrolysis. This exceptional performance can be ascribed to the synergetic effect of RuP_3 and CoP species, along with the unique morphologies and high surface area offered by NF. Furthermore, a catalytic mechanism of $NaBH_4$ hydrolysis on the Co-Ru-P@NF hybrid catalyst was purposed.

2. Experimental section

2.1. Synthesis of Co-species@NF

View Article Online
DOI: 10.1039/C8TA10695A

Co-species nanosheet arrays on NF (Ni foam) was prepared as follows, where a piece of NF (1 cm×1 cm×1.6 mm) was carefully pretreated in 1.0 M HCl, deionized water and ethanol for 5 min respectively. It was then repeated three times to confirm that the surface of NF was well cleaned.

To prepare the Co-species@NF, 1.0 mmol of $Co(NO_3)_2{\cdot}6H_2O$ was ultrasonically dissolved in 40 mL deionized water to form a uniform solution. The electrodeposition experiments were carried out at room temperature in a standard three-electrode system with NF as the working electrode, a Pt sheet as the counter electrode, and a standard SCE as the reference electrode. The applied current density was set as –10 mA cm^{-2}, and different electrodeposition times were conducted to control the amount of the Co-species (20, 30, 40, 50 and 60 min). The resulted samples were washed by abundant deionized water and dried in air at room temperature. The loadings of Co-species on NF surface are calculated for 3.67, 5.5, 7.34, 9.17 and 11.01 mg cm^{-2}, respectively.

2.2. Synthesis of CoRu-species@NF

50 mg of ruthenium(III) 2,4-pentanedionate was ultrasonically dispersed into 10 ml ethanol to form a homogeneous solution. Then, the mixture solution was pipetted onto the surface of Co-species@NF-60 and dried in air at room temperature. For a better comparison, different volumes of the precursors on the NF-60 surface are investigated. Moreover, the precursor covered fresh NF is also studied.

2.3. Synthesis of Co-Ru-P@NF by vapor phase phosphidation

The phosphidation process was performed in a tube furnace, where the NaH_2PO_2 in a porcelain boat was put in the upstream side and a series of CoRu-species/NF samples were placed next to the NaH_2PO_2 at a downstream side. The furnace was heated to 350 °C with 2 °C min^{-1} in Ar atmosphere (20 sccm), and kept at 350 °C for 2 h. After the phosphidation, the

samples were cooled down to ambient temperature in flowing Ar gas. As a comparison, the CoP@NF, RuP_3@NF and Ni_2P@NF were also prepared by a similar phosphidation process.

2.4. Catalyst characterizations

The crystal structures of catalysts were analyzed by X-ray powder diffraction (XRD, Rigaku D/Max 2500 V/PC) with a sweep speed for 2.0 degree min^{-1}. The morphologies and microstructures of the catalysts were characterized by scanning electron microscope (SEM, FEI Quanta 200 FEG) and transmission electron microscope (TEM, JEM-2100F). The X-ray photoelectron spectrometer (XPS, JPS-9010 Mg Kα) was used to analyze the chemical states of different elements. The specific surface area of the as-prepared product was measured on a Quantachrome Autosorb AS-1 instrument. The actual loadings of different metals in the catalyst were checked by inductive coupled plasma atomic emission spectroscopy (ICP-AES, IRIS Intrepid II XSP).

2.5. Catalytic measurements

The catalytic activity, cycle stability and activation energy of the catalytic material were obtained by the following methods. Typically, 50 mL mixture solution (contained 150 mM $NaBH_4$+0.4 wt% NaOH) was kept in a three-necked round-bottom flask (100 mL), which was placed in a water bath at 25 °C. The volume of H_2 was monitored by a drainage which was connected to a computer to record the instantly changed qualities of water. The catalytic reaction was started when the catalyst was added into the flask under constant magnetic stirring conditions. In order to test the recyclability of the catalyst, we continued to use the fresh $NaBH_4$ solution instead of the fully decomposed $NaBH_4$ solution for five consecutive cycles at 25 °C. After each stability test, we centrifuged the catalytic material, dried it under vacuum condition at room temperature, and weighed the catalytic material. All experiments were repeated three times to ensure the reliable results. The activation energy of the designed catalyst was evaluated in the same device in the temperature range of 25 to 45 °C.

View Article Online
DOI: 10.1039/C8TA10695A

The specific H_2 generation rate (HGR) and turnover frequency (TOF) values is calculated as follows,[34, 37]

$$HGR = \frac{V_{H_2O}\,(mL)}{t\,(\mathrm{min}) \times m\,(g)} \qquad (1)$$

$$TOF = \frac{n_{H_2}(mol)}{t\,(\mathrm{min}) \times n_{Ru}\,(\mathrm{mol})} \qquad (2)$$

where V_{H2O} is the volume of drained water, m is the total mass of the catalyst, n_{H2} is the moles of generated H_2, n_{Ru} is the moles of Ru in the catalyst, and t is the total reaction time in minutes.

3. Results and discussion

3.1. Synthetic strategy analysis

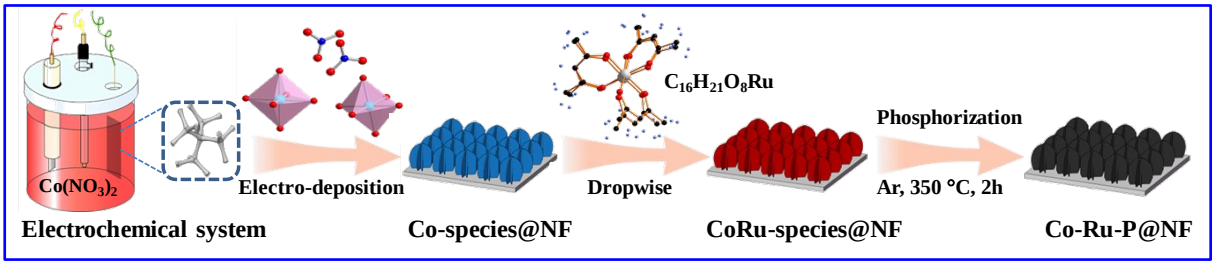

Fig. 1. Schematic diagram of the formation of Co-Ru-P@NF catalyst.

The three dimension Co-Ru-P@NF catalysts were prepared through three steps including electrodeposition of Co species, Ru modification and high-temperature phosphorization (**Fig. 1**). Initially, the Co-species were loaded on NF surface (Co@NF) by electrodeposition at a constant current density within various time lengths. Thereafter, Ru-precursors in ethanol solution were loaded dropwise onto the surface of Co@NF. Finally, the Ru loaded Co@NFs were placed in a porcelain boat next to another porcelain boat in the upside containing NaH_2PO_2 as phosphor sources. The hierarchically structured Co-Ru-P@NF materials were prepared through a vapor deposition of phosphorous under constant argon flow at 350 °C for 2

h. The metal loadings were determined by ICP-AES, which were used to calculate the TOF of H_2 generation (**Table S1**). Moreover, the pictures of the sample at different stages indicate the surface transformations by various chemical treatments as shown in **Fig. S1** and the weight changes of the catalysts were monitored using a precision balance to calculate the following H_2 generation rates (**Table S2**).

3.2. Crystal structures and microstructures analysis

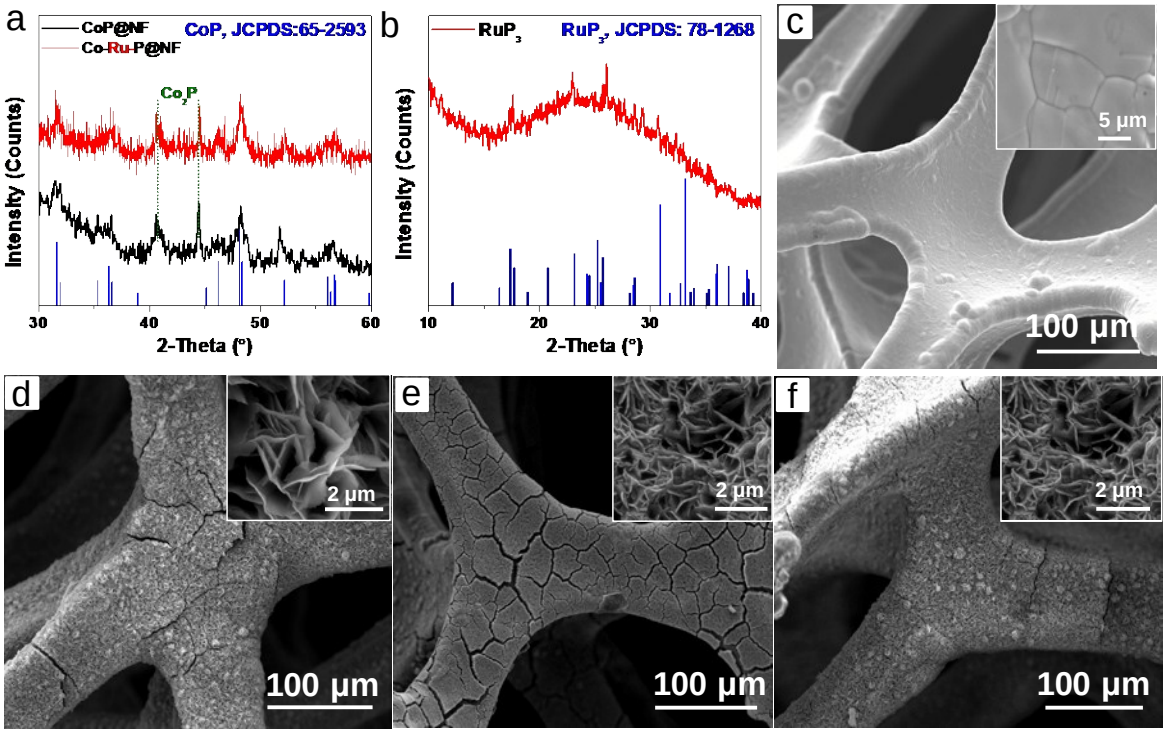

Fig. 2. X-ray diffraction (XRD) patterns of (a) CoP@NF and Co-Ru-P@NF along with (b) RuP_3. Scanning electron microscopy (SEM) images of (c) NF, (d) Co-species@NF, (e) CoP@NF and (f) Co-Ru-P@NF. The inserts are the magnified SEM images.

The crystal structures of as-prepared materials are initially investigated by XRD patterns. As shown in **Fig. S2**a, the electrodeposited Co-species on NF surface are consistent with the standard XRD features of $Co(OH)_2$ (JCPDS: 30-0443).[38] After phosphorization process, the color of Co@NF changed from dark blue to black. The cobalt phosphate species mainly

View Article Online
DOI: 10.1039/C8TA10695A

consists of CoP (JCPDS: 65-2593)[39] and a trace of Co_2P species (JCPDS: 54-0413), where the XRD patterns of the Ru species cannot be detected due to the low Ru loading as shown in **Fig. 2**a. However, the pure Ru-species which were synthesized by similar conditions were detected by the XRD pattern in **Fig. 2**b and the patterns are consistent with RuP_3 (JCPDS: 78-1268). In addition, the NF was phosphatized and used as a control sample. Small amounts of Ni_2P species (JCPDS: 03-0953) formed on the NF surface (**Fig. S2**b). Moreover, none of the diffraction peaks of NF and Ni_2P appeared on Co modified NF indicating a full surface coverage of NF. Therefore, the contribution of Ni_2P towards the catalytic performance of RuP_3-CoP is negligible. As shown in **Fig. 2**c, the SEM images are used to distinguish the morphological changes of NF before and after deposition. The surface morphology of NF changes dramatically from the relatively smooth surface to highly ring coiled hierarchical structures in micro level after different electrodeposition times, indicating the formation of $Co(OH)_2$ nanosheets on NF surface which becomes denser upon increase of the deposition time (**Fig. S3**, **Fig. 2**d). After phosphorization at 350 ^{o}C, the vertically oriented hierarchical structure starts to shrink because of the crystal structure transformation from amorphous to crystalline. The similar phenomena are observed on both CoP@NF and Co-Ru-P@NF (**Fig. 2**e and **2**f). The hierarchical structures not only provide the high surface area thereby promoting a better mass transfer but also exposes more active sites. Therefore, a high catalytic performance is expected. Moreover, the N_2 adsorption–desorption isotherms at 77 K of Co-Ru-P@NF catalysts with different loadings of Ru species were used to investigate the Brunauer–Emmett–Teller (BET) surface area. The results revealed that when the loading of Ru in the Co-Ru-P@NF is 0.197 mg cm^{-2}, the BET surface area is 11.4 m^2 g^{-1}, and when the loading of Ru is 0.455 mg cm^{-2}, the BET surface area is 13.3 m^2 g^{-1} (**Fig. S4**).

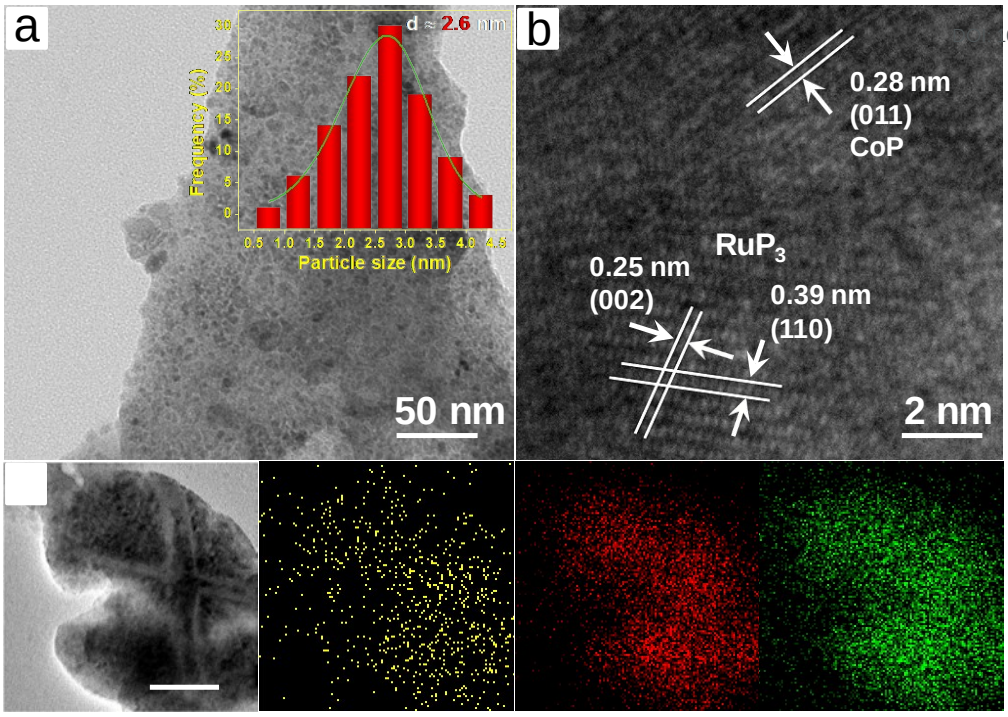

Fig. 3. (a) Transmission electron microscopy (TEM) and (b) high-resolution TEM images of Co-Ru-P material. The inset of Fig. 3a represents the particle size distribution of RuP_3. (c) Typical TEM image of Co-Ru-P and the corresponding Ru, Co and P elemental mappings.

To further examine the microscopic features of the Co-Ru-P@NF, detailed TEM studies were undertaken. As shown in **Fig. 3**a, the RuP_3 nanoclusters with an average particle size of 2.6 nm are uniformly dispersed on the surface of CoP nanosheet. The crystal structures of both CoP and RuP_3 are confirmed in **Fig. 3**b where the distinct lattice fringe with a spacing of 0.28 nm is corresponding to the (111) plane of CoP, and the two closely related spacings of 0.25 and 0.39 nm are attributed to the (002) and (110) planes of RuP_3, respectively. Furthermore, the HAADF-STEM (**Fig. 3**c) and corresponding elemental mapping images reveal the homogenous distribution of Ru, Co, and P in the Co-Ru-P nanostructures. Notably, the much sparser Ru dispersion patterns are consistent with features the low content Ru-based material in the hybrid composite.

3.3. XPS analysis

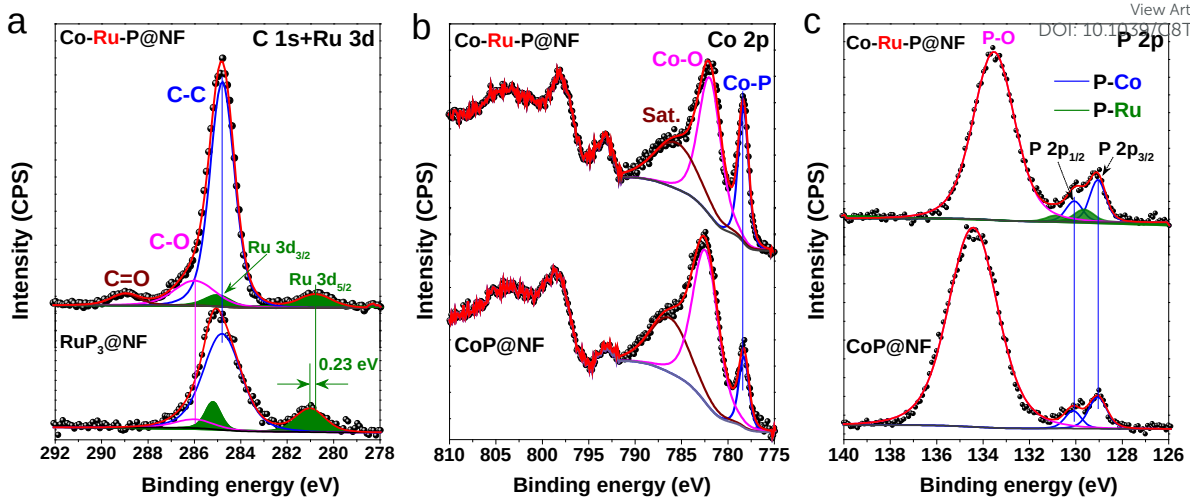

Fig. 4. High-resolution X-ray photoelectron spectroscopy (XPS) of (a) C 1s + Ru 3d, (b) Co 2p and (c) P 2p regions from Co-Ru-P@NF, RuP_3@NF and CoP@NF.

The chemical states of each elements in Co-Ru-P@NF are further analyzed by XPS, where the Ni cannot be detected on the surface of the Co-Ru-P@NF (**Fig. S5**), which not only shows a uniform deposition of Co but also indicates the Co film is thicker that the penetration depth of XPS (around 10 nm). The high-resolution XPS spectra of C 1s + Ru 3d regions (**Fig. 4**a) are convoluted into C-C (284.8 eV) and C-O (286.0 eV) used as a calibration standard,[40, 41] as well as the Ru 3d core level from RuP_3 are convoluted at the binding energies of 280.8 eV (Ru $3d_{5/2}$) and 285.0 eV (Ru $3d_{3/2}$).[42] As shown in **Fig. 4**b, three peaks in the Co $2p_{3/2}$ regions at 778.3, 782.0 and 785.5 eV can be ascribed to the Co-P, Co-O and satellite peaks, respectively.[43] In addition, the high-resolution XPS spectrum of P 2p core level shows three types of peaks, where a pair of peaks located at 129.1 eV (P $2p_{3/2}$) and 130.1 eV (P $2p_{1/2}$) are considered as P 2p in CoP.[44] The another pair of peaks located at 129.7 eV (P $2p_{3/2}$) and 130.8 eV (P $2p_{1/2}$) are attributed to P 2p in RuP_3,[45] along with a broad peak at 133.6 eV is assigned to phosphate species.[46] These distinct oxidation species peaks of Co-O and P-O can be explained by the inevitable surface oxidation.[47] We have compared the high-resolution Ru 3d XPS spectra of RuP_3@NF and Co-Ru-P@NF in **Fig. 4**a. The results show that the binding energy of Ru 3d of

Co-Ru-P@NF exhibits a negative shift of ca. 0.23 eV compared to that of RuP_3@NF indicating higher electron density on Ru in the Co-Ru-P@NF as compare to that of RuP_3@NF due to the partial electron transfer from Co species indicating that the electron density on Ru species is lower than that of Co species. However, almost no shift was observed in the case of Co 2P because Ru amounts are so small consequently the charge transfer is not significant enough to cause the shift on Co 2P signal.

3.4. Catalytic hydrolysis analysis

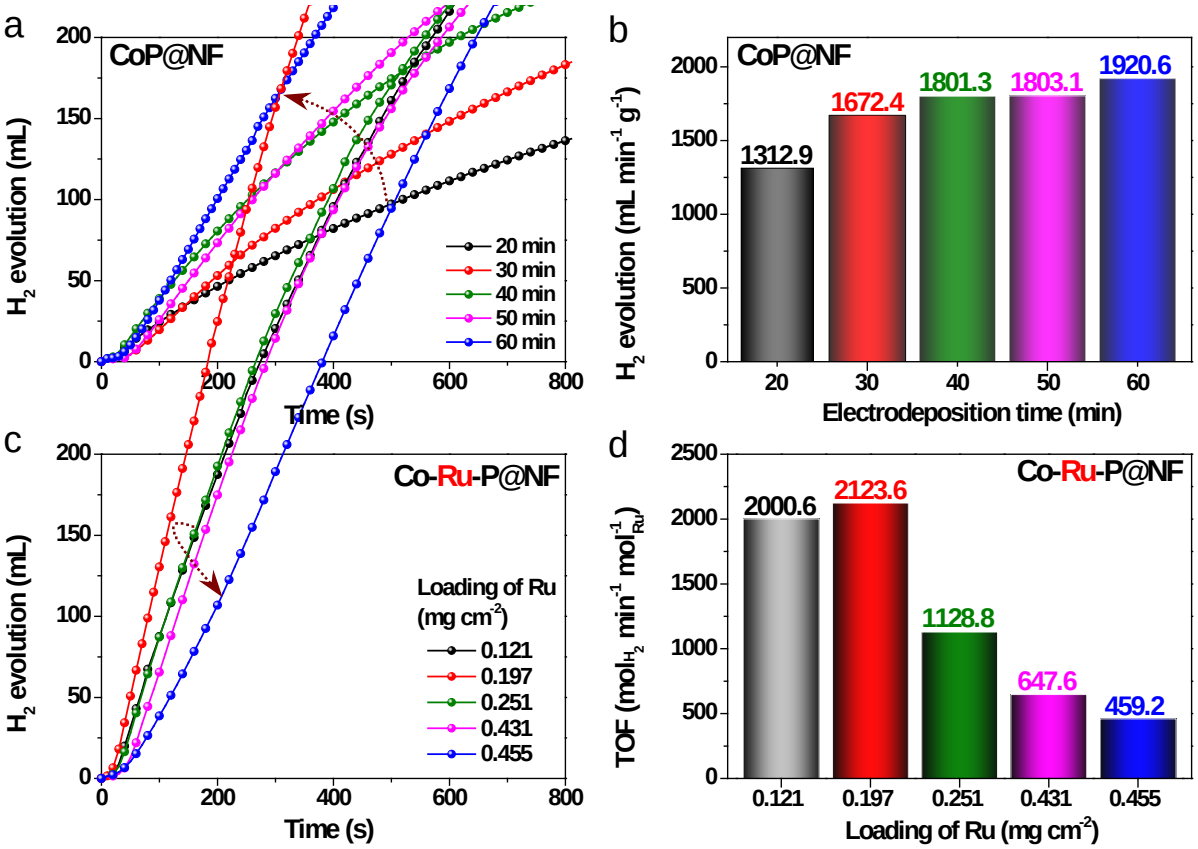

Fig. 5. (a) The relationship between the H_2 generation rates and electro-deposition times of CoP@NF catalysts, and (b) the summarized TOF values. (c) The relationship between the H_2 generation rates and loadings of Ru species on Co-Ru-P@NF catalysts, and (d) the summarized TOF values. All the experiment are conducted in 150 mM $NaBH_4$ + 0.4 wt % NaOH at 25 °C.

View Article Online
DOI: 10.1039/C8TA10695A

The H_2 production of $NaBH_4$ hydrolysis using the designed catalysts were performed in alkalized $NaBH_4$ solution at 25 °C. The schematic illustration of the experimental setup is shown in **Fig. S6**, where the amounts of the generated H_2 was calculated according to the weight of the water displaced by H_2. The effect of electrodeposition of CoP at various time on the H_2 production was investigated in **Fig. 5**a-b. The results show that the H_2 generation rate is gradually increased with the prolonged deposition times and the 60 min deposition time was selected as the basis of all the other experiments performed blow. In addition, the optimal Ru loading was investigated by altering the deposition methods such as drop casting and dip coating as well as the use of several Ru precursors including $C_{15}H_{21}O_6$ Ru, $RuCl_2$ and Ru nanoparticles (**Fig. S7**). Then, the catalytic performance of the resulting catalysts on H_2 generation was monitored (**Fig. S8**). Finally, the best catalytic performance was achieved by using ethanol solution of $C_{15}H_{21}O_6Ru$ through drop casting method. The optimal loading is around 0.2 mg (Ru)/cm^2 measured by ICP-AES (**Table S1-S2**) and the overall Ru loading against Co is around 1.57 wt% (0.09% mole%). The corresponding TOF to the fastest hydrogen evolution rate (4840 mL min^{-1} g^{-1} catalyst) is 2123.6 mol min^{-1} mol$_{Ru}^{-1}$, which is the highest TOF value reported so far among all the $NaBH_4$ hydrolysis catalysts (**Table S3**). This outstanding catalytic performance can be related to the high surface roughness that exposes more active sites, uniform distribution of the active sites and synergic effect between Ru and Co.

To further evaluate this synergetic effect, a comparison study of $NaBH_4$ decomposition was performed between all the intermediate catalysts including CoP@NF, RuP_3@NF, Co-species@NF, Ni_2P@NF and NF. The results show that the hydrogen generation rate of 1.57 wt% Ru loaded CoP@NF is significantly higher than that of CoP@NF and RuP_3@NF (**Fig. S9**). Meanwhile, the NF and Ni_2P@NF show almost no activity towards H_2 generation towards $NaBH_4$ hydrolysis **(Fig. 6**a). The specific H_2 evolution rate of Co-Ru-P@NF is 4839.8 mL min^{-}

View Article Online
DOI: 10.1039/C8TA10695A

[1] g_{cat}^{-1} (total mass of catalyst), which are 2.52 and 23.55 folds higher than those of CoP@NF and RuP_3@NF respectively. To measure the activation energies, a set of experiments were conducted at different temperatures using the two most active catalysts such as the Co-Ru-P@NF and the CoP@NF. As shown in **Fig. S10-S11**, the rate of H_2 generation increases rapidly with increasing the reaction temperatures from 298 K to 318 K, and the rate constant κ is calculated from the initial slope of each experiment. The activation energy of Co-Ru-P@NF catalyst is calculated to be 40.3 kJ mol^{-1} by the Arrhenius plot (ln κ *vs* 1/T), which is much lower than that of CoP@NF (56.1 kJ mol^{-1}) (**Fig. 6**b), implying a kinetically enhanced catalytic activity towards $NaBH_4$ hydrolysis to produce H_2 owing to the Ru.[48]

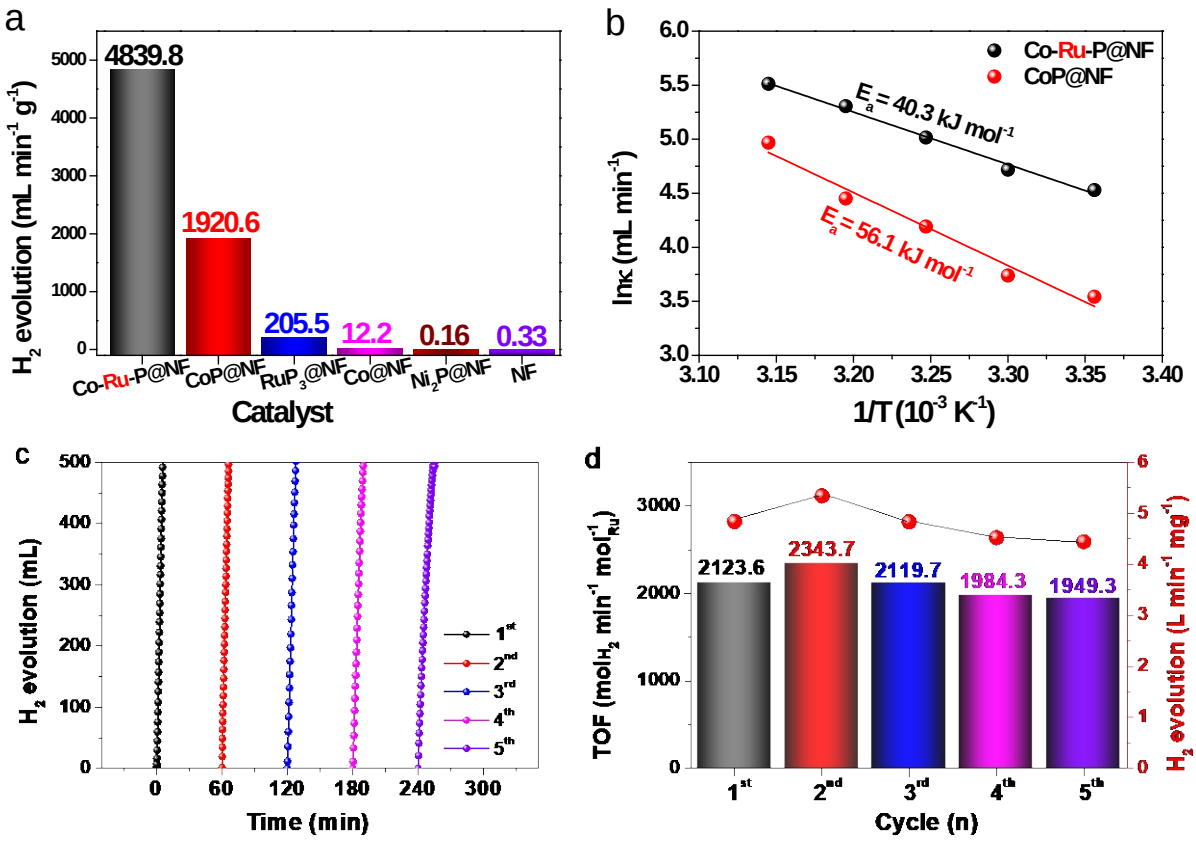

Fig. 6. (a) The summarized TOF values of different catalysts for hydrolysis of 150 mM $NaBH_4$ + 0.4 wt % NaOH solution at 25 °C. (b) The summarized Arrhenius plots of CoP@NF and Co-Ru-P@NF at different reaction temperatures for alkalized $NaBH_4$ hydrolysis. (c) Recycling stability test of the Co-Ru-P@NF catalyst in 150 mM $NaBH_4$ + 0.4 wt % NaOH at 25 °C. (b)

View Article Online
DOI: 10.1039/C8TA10695A

The specific H_2 evolution rates and the corresponding TOF values of Co-Ru-P@NF catalyst in the different recycling test.

The stability of the optimized Co-Ru-P@NF catalyst was evaluated by the continuous recycling experiments of the $NaBH_4$ hydrolysis in basic solution. The catalyst was cleaned, freeze-dried and weighed after each cycle. The results show almost no changes in catalytic performance after five consecutive cycles after normalizing to the catalyst-mass (**Fig. 6**c-d). However, the time required to reach the 500 mL of H_2 was increased from 5.9 to 13.9 min after five cycles. The catalyst deactivation could be ascribed to the RuP_3 exfoliation, structural damages and catalyst poisoning by BO_2^- species (**Fig. S12-S13**).[49]

3.5. Catalytic mechanism analysis

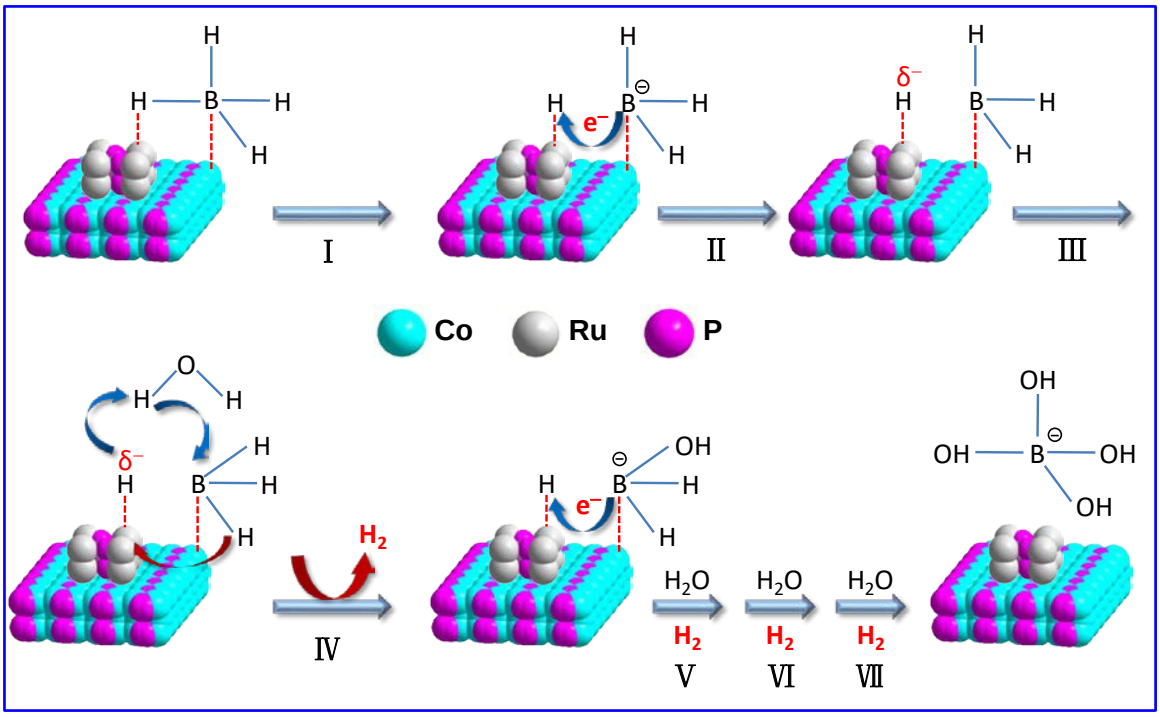

Fig. 7. Catalytic mechanism diagram of the Co-Ru-P@NF catalyst for H_2 generation by hydrolysis of alkalized $NaBH_4$ solution.

View Article Online
DOI: 10.1039/C9TA10695A

As mentioned above, the high catalytic activities of Co-Ru-P@NF series are directly related to the synergetic effect between Ru and Co along with the unique morphology associated with the large surface area and the open-channels for effective mass transport. The negative shift of the Ru 3d binding energy in XPS caused by the partial electron transfer from Co species to Ru species indicates a higher electron density on Co species as compared to that of Ru species. Accordingly, the partially electron negative hydrogen atoms preferred to attach to the Ru^{3+} atoms. As a result, the BH_4^- goes a reversible dissociation on Co and Ru metal sites where the hydrogen atom adsorbs on Ru and BH_3 attaches to the Co species. The negatively charged boron species transfer the electron to Ru through the conductive balk and then the partially negatively charged hydrogen atom on the Ru surface extracts a hydrogen from water while the OH ion attacks the BH_3 to release the H_2 molecule followed by transferring one hydrogen atom of the BH_3 to the free Ru site. The surface adsorbed $BH_2(OH)$ species forms after one cycle. The reaction continues until all the hydrogen atoms are replaced by OH ions and then the $B(OH)_4^-$ leaves the surface.[50]

4. Conclusion

In summary, we have successfully developed a simple and novel strategy to fabricate hierarchically structure of RuP_3 loaded CoP@NF nanosheets for H_2 generation from $NaBH_4$ hydrolysis in alkaline solution. The XRD, XPS and TEM analysis of the Co-Ru-P@NF material show that the RuP_3 nanoclusters are uniformly dispersed on the surface of vertically grown CoP nanosheets on the NF, which creates the channels for rapid mass transfer and sufficient exposure of the active sites. The resulted Co-Ru-P@NF catalyst exhibits an exceptionally high TOF value of 2123.6 mol_{H2} min^{-1} mol^{-1}_{Ru} at 25 °C, which is one of the highest result reported so far. The superior catalytic activity is a strong agreement with the low activation energy (40.3 kJ mol^{-1}). Additionally, the Co-Ru-P@NF catalyst shown a slight decay

around 8.2% after five cycles demonstrating a good stability towards $NaBH_4$ hydrolysis. Furthermore, this study might shed light on designing a metal-phosphide based catalyst for $NaBH_4$ hydrolysis as a high activity, good durability, and reusability.

Acknowledgements

This work has been supported by the National Natural Science Foundation of China (21363003, 21165004, 21163002), Natural Science Foundation of Guangxi Province (2014GXNSFGA118008, 2014GXNSFFA118003), BAGUI scholar program (2014A001) and Project of Talents Highland of Guangxi Province.

Appendix A. Supplementary data

Figs. S1-S13 and Tables S1-S3 give more details on characterization of our synthesized materials and their catalytic performance data; additional photograph, XRD, SEM, XPS and catalytic performance data (PDF).

Conflicts of interest

There are no conflicts to declare.

Notes and references

1. X. Zhang, Y. Zhao, X. Jia, Y. Zhao, L. Shang, Q. Wang, G. I. N. Waterhouse, L.-Z. Wu, C.-H. Tung and T. Zhang, *Adv. Energy Mater.*, 2018, **8**, 1702780.
2. J. Chen, Z.-H. Lu, Q. Yao, G. Feng and Y. Luo, *J. Mater. Chem. A*, 2018, **6**, 20746-20752.
3. D. G. Tong, D. M. Tang, W. Chu, G. F. Gu and P. Wu, *J. Mater. Chem. A*, 2013, **1**, 6425-6432.
4. N. Sahiner and S. Demirci, *Appl. Catal. B: Environ.*, 2017, **202**, 199-206.
5. T. Liu, K. Wang, G. Du, A. M. Asiri and X. Sun, *J. Mater. Chem. A*, 2016, **4**, 13053-13057.
6. H.-L. Wang, J.-M. Yan, Z.-L. Wang, S.-I. O and Q. Jiang, *J. Mater. Chem. A*, 2013, **1**, 14957-14962.
7. Y. Li, T. Gao, Y. Yao, Z. Liu, Y. Kuang, C. Chen, J. Song, S. Xu, E. M. Hitz, B. Liu, R. J. Jacob, M. R. Zachariah, G. Wang and L. Hu, *Adv. Energy Mater.*, 2018, **8**, 1801289.

8. C. Tang, L. Xie, K. Wang, G. Du, A. M. Asiri, Y. Luo and X. Sun, *J. Mater. Chem. A*, 2016, **4**, 12407-12410.
9. Q. Yao, Z.-H. Lu, W. Huang, X. Chen and J. Zhu, *J. Mater. Chem. A*, 2016, **4**, 8579-8583.
10. F. Fu, C. Wang, Q. Wang, A. M. Martinez-Villacorta, A. Escobar, H. Chong, X. Wang, S. Moya, L. Salmon, E. Fouquet, J. Ruiz and D. Astruc, *J. Am. Chem. Soc.*, 2018, **140**, 10034–10042.
11. H. Zhang, G. Xia, J. Zhang, D. Sun, Z. Guo and X. Yu, *Adv. Energy Mater.*, 2018, **8**, 1702975.
12. Z. Zhang, S. Zhang, Q. Yao, X. Chen and Z.-H. Lu, *Inorg. Chem.*, 2017, **56**, 11938-11945.
13. A. Kantürk Figen, K. Taşçi and B. Coşkuner Filiz, *Kinet. Catal.*, 2018, **59**, 128-135.
14. C. Wu, J. Zhang, J. Guo, L. Sun, J. Ming, H. Dong, Y. Zhao, J. Tian and X. Yang, *ACS Sustain. Chem. Eng.*, 2018, **6**, 7451–7457.
15. C. Wu, J. Guo, J. Zhang, Y. Zhao, J. Tian, T. T. Isimjan and X. Yang, *Renew. Energy*, 2018, DOI: doi.org/10.1016/j.renene.2018.09.070, doi.org/10.1016/j.renene.2018.1009.1070.
16. A. Lale, A. Wasan, R. Kumar, P. Miele, U. B. Demirci and S. Bernard, *Int. J. Hydrog. Energy*, 2016, **41**, 15477-15488.
17. J.-X. Kang, T.-W. Chen, D.-F. Zhang and L. Guo, *Nano Energy*, 2016, **23**, 145-152.
18. M. Irum, M. Zaheer, M. Friedrich and R. Kempe, *RSC Adv.*, 2016, **6**, 10438-10441.
19. Q. Yao, W. Shi, G. Feng, Z.-H. Lu, X. Zhang, D. Tao, D. Kong and X. Chen, *J. Power Sources*, 2014, **257**, 293-299.
20. H. X. Nunes, M. J. F. Ferreira, C. M. Rangel and A. M. F. R. Pinto, *Int. J. Hydrogen Energy*, 2016, **41**, 15426-15432.
21. L. Wang, L. Huang, C. Jiao, Z. Huang, F. Liang, S. Liu, Y. Wang and H. Zhang, *Catalysts*, 2017, **7**, 25.
22. L. Wei and Z. Yuan, *AIP Conf. Proc.*, 2017, **1794**, 020004.
23. C. Li, D. Wang, Y. Wang, G. Li, G. Hu, S. Wu, Z. Cao and K. Zhang, *J. Colloid Interface Sci.*, 2018, **524**, 25-31.
24. F. Wang, Y. Zhang, Y. Wang, Y. Luo, Y. Chen and H. Zhu, *Int. J. Hydrogen Energy*, 2018, **43**, 8805-8814.
25. Y. Zou, Y. Yin, Y. Gao, C. Xiang, H. Chu, S. Qiu, E. Yan, F. Xu and L. Sun, *Int. J. Hydrogen Energy*, 2018, **43**, 4912-4921.
26. Q. Li, W. Yang, F. Li, A. Cui and J. Hong, *Int. J. Hydrog. Energy*, 2018, **43**, 271-282.
27. K. A. Holbrook and P. J. Twist, *J. Chem. Soc. A*, 1971, **0**, 890-894.
28. C.-C. Hou, Q. Li, C. Wang, C.-Y. Peng, Q.-Q. Chen, H.-F. Ye, W. Fu, C.-M. Che and N. Lopez, *Energy Environ. Sci.*, 2017, **10**, 1770-1776.
29. C. Tang, R. Zhang, W. Lu, L. He, X. Jiang, A. M. Asiri and X. Sun, *Adv. Mater.*, 2017, **29**, 1602441.
30. Y. Wei, Y. Wang, L. Wei, X. Zhao, X. Zhou and H. Liu, *Int. J. Hydrog. Energy*, 2018, **43**, 592-600.
31. L. He, D. Zhou, Y. Lin, R. Ge, X. Hou, X. Sun and C. Zheng, *ACS Catal.*, 2018, **8**, 3859-3864.
32. A. H. Tamboli, S. W. Gosavi, C. Terashima, A. Fujishima, A. A. Pawar and H. Kim, *Chemosphere*, 2018, **202**, 669-676.
33. X. Peng, D. Chen, X. Yang, D. Wang, M. Li, C.-C. Tseng, R. Panneerselvam, X. Wang, W. Hu, J. Tian and Y. Zhao, *ACS Appl. Mater. Interfaces*, 2016, **8**, 33673-33680.
34. L. Cui, Y. Xu, L. Niu, W. Yang and J. Liu, *Nano Res.*, 2017, **10**, 595-604.

View Article Online
DOI: 10.1039/C8TA10695A

35. L. Wei, M. Ma, Y. Lu, S. Zhang, J. Gao and X. Dong, *Funct. Mater. Lett.*, 2017, **10**, 1750065.
36. K. Mori, K. Miyawaki and H. Yamashita, *ACS Catal.*, 2016, **6**, 3128-3135.
37. Q. Yao, Z.-H. Lu, Y. Yang, Y. Chen, X. Chen and H.-L. Jiang, *Nano Res.*, 2018, **11**, 4412-4422.
38. X. Yang, H. Li, A.-Y. Lu, S. Min, Z. Idriss, M. N. Hedhili, K.-W. Huang, H. Idriss and L.-J. Li, *Nano Energy*, 2016, **25**, 42-50.
39. X. Yang, A.-Y. Lu, Y. Zhu, M. N. Hedhili, S. Min, K.-W. Huang, Y. Han and L.-J. Li, *Nano Energy*, 2015, **15**, 634-641.
40. T. Tang, Q. Gan, X. Guo, H. Dong, J. Zhang, Y. Zhao, J. Tian and X. Yang, *Sustain. Energ. Fuels*, 2018, **2**, 229-236.
41. Y. Zeng, S. Tian, D. Wang, H. Dong, X. Cheng, Y. Zhao, J. Tian and X. Yang, *ChemistrySelect*, 2017, **2**, 9291-9297.
42. C. Jing-Qi, G. Wen-Kun, L. Jia-Hui, D. Bin, Y. Kai-Li, Q. Jun-Feng, L. Bin, C. Yong-Ming and L. Chen-Guang, *ChemSusChem*, 2018, **11**, 743-752.
43. S. Liu, Q. Liu, Y. Lv, B. Chen, Q. Zhou, L. Wang, Q. Zheng, C. Che and C. Chen, *Chem. Commun.*, 2017, **53**, 13153-13156
44. W. Gao, M. Yan, H.-Y. Cheung, Z. Xia, X. Zhou, Y. Qin, C.-Y. Wong, Y. Qu, C.-R. Chang and J. C. Ho, *Nano Energy*, 2017, **38**, 290-296.
45. Z. Pu, I. S. Amiinu, Z. Kou, W. Li and S. Mu, *Angew. Chem.-Int. Edit.*, 2017, **56**, 11559-11564.
46. H. Zhang, X. Li, A. Hähnel, V. Naumann, C. Lin, S. Azimi, S. L. Schweizer, A. W. Maijenburg and R. B. Wehrspohn, *Adv. Funct. Mater.*, 2018, **28**, 1706847.
47. S. Cao, Y. Chen, H. Wang, J. Chen, X. Shi, H. Li, P. Cheng, X. Liu, M. Liu and L. Piao, *Joule*, 2018, **2**, 549-557.
48. D. Kılınç, Ö. Şahin and C. Saka, *Int. J. Hydrog. Energy*, 2018, **43**, 251-261.
49. L. Zhou, J. Meng, P. Li, Z. Tao, L. Mai and J. Chen, *Mater. Horizons*, 2017, **4**, 268-273.
50. U. B. Demirci and P. Miele, *C. R. Chim.*, 2014, **17**, 707-716.